remote sensing

MDPI

Article

Remote Sensing Exploration of Nb-Ta-LREE-Enriched Carbonatite (Epembe/Namibia) †

Robert Zimmermann [1,*], Melanie Brandmeier [1], Louis Andreani [2], Kombada Mhopjeni [3] and Richard Gloaguen [1]

1 Helmholtz-Zentrum Dresden-Rossendorf, Helmholtz Institute Freiberg for Resource Technology, Division "Exploration Technology", Chemnitzer Str. 40, 09599 Freiberg, Germany; melanie.brandmeier@gmx.de (M.B.); r.gloaguen@hzdr.de (R.G.)

2 TU Bergakademie Freiberg, Institute of Geology, Bernhard-von-Cotta-Str. 2, 09599 Freiberg, Germany; andreani.louis@googlemail.com

3 Geological Survey of Namibia, 1 Aviation Road, Windhoek, Namibia; kombada.mhopjeni@mme.gov.na

* Correspondence: r.zimmermann@hzdr.de; Tel.: +49-351-260-4431

† This paper is an extended version of our paper published in Geophysical Research Abstracts, Volume 17, EGU2015-8836-1, 2015.

Academic Editors: Lenio Soares Galvao and Prasad S. Thenkabail
Received: 30 June 2016; Accepted: 22 July 2016; Published: 28 July 2016

Abstract: On the example of the Epembe carbonatite-hosted Nb-Ta-LREE deposit, we demonstrate the use of hyperspectral reflectance data and geomorphic indicators for improving the accuracy of remote sensing exploration data of structurally-controlled critical raw material deposits. The results further show how exploration can benefit from a combination of expert knowledge and remotely-sensed relief, as well as imaging data. In the first stage, multi-source remote sensing data were used in lithological mapping based on Kohonen Self-Organizing Maps (SOM). We exemplify that morphological indices, such as Topographic Position Index (TPI), and spatial coordinates are crucial parameters to improve the accuracy of carbonate classification as much as 10%. The resulting lithological map shows the spatial distribution of the ridge forming carbonatite dyke, the fenitization zone, syenite plugs and mafic intrusions. In a second step, the internal zones of the carbonatite complex were identified using the Multi-Range Spectral Feature Fitting (MRSFF) algorithm and a specific decision tree. This approach allowed detecting potential enrichment zones characterized by an abundance of fluorapatite and pyroxene, as well as dolomite-carbonatite (beforsite). Cross-validation of the mineral map with field observations and radiometric data confirms the accuracy of the proposed method.

Keywords: carbonatite; REE; self-organizing maps; decision tree; spectral feature fitting; geomorphology; Namibia; HyMap; SRTM

1. Introduction

The Epembe carbonatite is Namibia's largest carbonatite complex with an extent of 7000 × 400 m. This fault-controlled søvite (calcio-carbonatite [1]) dyke is of Paleoproterozoic age and is currently being explored for Ta, Nb and Light Rare Earth Elements (LREE) [2]. Due to sparse vegetation and good accessibility, it constitutes an ideal setting to evaluate the joint use of spectral and geometrical data for lithological mapping.

There is a wealth of publications describing methods and applications of different sensors and datasets (e.g., [3–8]) for remote sensing mineral exploration. Expert knowledge is often required to get reliable results if the target is rather small [9,10]. However, applications of remote sensing for the exploration of carbonatite were only tested in a few studies ([9,11–17]). Thus, there is a need to

improve remote sensing exploration techniques for REEs, Nb and Ta due to an increasing demand during the past few decades and the acceleration of this demand due to their augmenting use in high-tech industry ([18,19]).

Existing studies focus on mapping the extent of the carbonatite bodies and their alteration aureoles using (un-)supervised classification algorithms, as well as spectral unmixing techniques for mineral mapping. The methods used in most of these studies are confronted with problems in recognizing linear features or differentiating surface material having similar spectral signatures. The recognition of small-scale features, however, is very important for REE exploration, as enrichment often occurs within small dykes or distinct enrichment zones [20]. To tackle these problems, we use an approach that combines these spectral data with morphometric indices, which allow one to differentiate lithologies based on their distinct topographic signature (e.g., Othman and Gloaguen [21]).

In the first part of the paper, we use an unsupervised classification algorithm (Kohonen Self-Organizing Maps) for lithological mapping of carbonatite and enrichment zones. On the basis of the classification results obtained, methods to map enrichment zones within carbonatite sequences were evaluated in a second step. Limitations due to sub-economic REE enrichment at Epembe ($\sim$0.5% TREO+Y) and high detection limits (e.g., for Nd^{3+} $\sim$300 ppm in laboratory data [11]) were circumvented by the use of indicator minerals (e.g., see Mackay et al. [22] or Bull [23]), like apatite or a specific type of pyroxene (e.g., aegirine or augite), to estimate the Nb-Ta-REE potential of the deposit. Those low REE abundances also disable the use of deconvolution algorithms, as proposed by Neave et al. [17] or Boesche et al. [16]. The indicator mineral approach, however, cannot be generalized to all carbonatites, but a similar approach as presented here is advised.

Thus, on the example of the Epembe prospect, we exemplify (1) the positive impact of morphometric and spatial parameters on classification results and (2) the significance of expert-knowledge for the definition of detectable indicators for enrichment; as well as (3) present a multi-step classification approach that might be used on similar geological settings as a first step of exploration.

2. Geological Setting

The Epembe Complex (see Figure 1) is located in NW Namibia at the southern margin of the Kunene Intrusive Complex (KIC [24]). The KIC is a large, Paleoproterozoic, multi-stage mafic intrusion (anorthosite and related rocks [25]) at the southern margin of the Angola craton. In a late stage of the evolution of the KIC, a nearly complete sequence of pyroxenite, syenite and carbonatite intruded into the upper metamorphic basement (granulites, gneisses and amphibolites [26]).

The carbonatite-syenite composite body has an age of 1216 $\pm$ 2.4 Ma [27] and is hosted in a sub-vertical NW-SE trending dextral regional shear zone ([26,28]). The carbonatite is mainly made of calcio-carbonatite (søvite) with narrow zones of dolomite-carbonatite (beforsite [29]) indicating different phases of intrusion and/or hydrothermal overprint [1]. Modal mineralogy consists of carbonate minerals (mainly calcite, minor dolomite and ankerite) with aegirine, apatite and pyrochlore as accessories in the high-grade zones ([23,28]). Overall, an inhomogeneous ductile deformation strikes more or less parallel to the dyke. Deformation is strongest in the central part of the structure [29]. The carbonatite exhibits brittle deformation structures related to subsequent fault movements. Strong foliation of the carbonatite dipping 280/80 correlates with the general trend of the dominant shear zone and regional structural trends [23]. Internal structures with lenses of syenite and sub-parallel zones of different carbonatite facies, acquired during successive intrusive and hydrothermal episodes [29], are exhibited. Flow bands containing accessory minerals indicate REE mineralization occurring during a late-stage hydrothermal event [28]. Mineralization is primarily associated with pyrochlore for Nb and Ta, as well as monazite, apatite and synchysite for REE. Several high grade zones (up to a few meters wide) with the highest levels of 250 ppm Ta_2O_5 and 900 ppm Nb_2O_5 ([2]; Sector B), are characterized by both a higher abundance of apatite as an REE-bearing phase and a higher abundance of pyroxene [23]. These phases can thus be used as

indicator minerals for enrichment zones. A positive correlation of these zones with high U- and K-count rates allows the use of these measurements for cross-validation, as discussed later [28]. This is to some extent related to the substitution of U in pyrochlore [30] and to the hydrothermal overprint and formation of alteration minerals (e.g., clays; high K dose rates [31]).

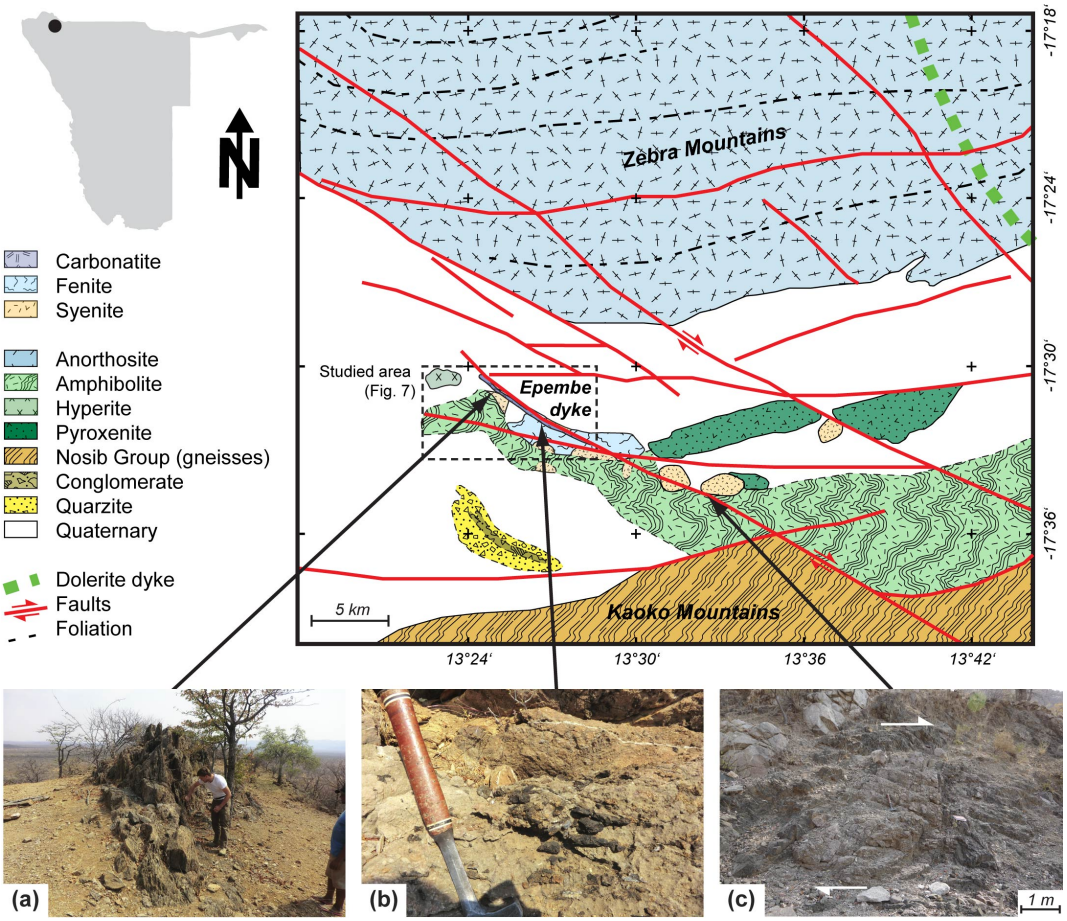

Figure 1. Location of the study area in Namibia and simplified geological map of Epembe (Geological Survey of Namibia, Sheet Swartbooisdrift) modified after Maier et al. [24]. Faults are compiled from Maier et al. [24] and IBML [2]. The extension of the classified study area is marked with a dashed rectangle. Field images below: (**a**) Epembe Sector B: carbonatite is forming small ridges; (**b**) Epembe Sector B: carbonatite outcrop with pseudomorphoses of aegirine (large black crystals) and apatite (small yellowish crystals); (**c**) Huge dextral shear zone with block rotation bounding the syenite intrusion to the southeast of Epembe carbonatite. The same shear zone hosts the carbonatite.

3. Spectral Reflectance Properties and Mineralogical Composition

3.1. Carbonatite

The term carbonatite is defined as a rock containing more than 50 modal% carbonate minerals (e.g., calcite, dolomite, ankerite or siderite [1]). A carbonatite is called rare earth carbonatite if the Total Rare Earth Oxide (TREO) content exceeds 1 wt % [1]. Carbonatites adjacent to complex, multi-stage intrusions may also show enrichment in Nb and Ta [32]. High levels of U and Th are often associated with Ta enrichment in early pyrochlore [30]. The Epembe carbonatite can be classified as calcio-carbonatite (or søvite).

Modal mineralogy consists of variable grain size carbonate (mainly calcite), pyroxene (aegirine), pyrochlore, REE-bearing apatite and REE minerals (e.g., monazite, allanite, bastnaesite and synchysite; see Figure 2a–c). Flow bands of aegirine and apatite are common and follow the general

strike of the dyke ([23,29]). Remanent crystals of aegirine, apatite and pyrochlore are evident on weathered surfaces of these bands. Nb-Ta-REE enrichment is assigned to a specific carbonatite type rich in apatite (ap) and pyroxene (px) [23,29].

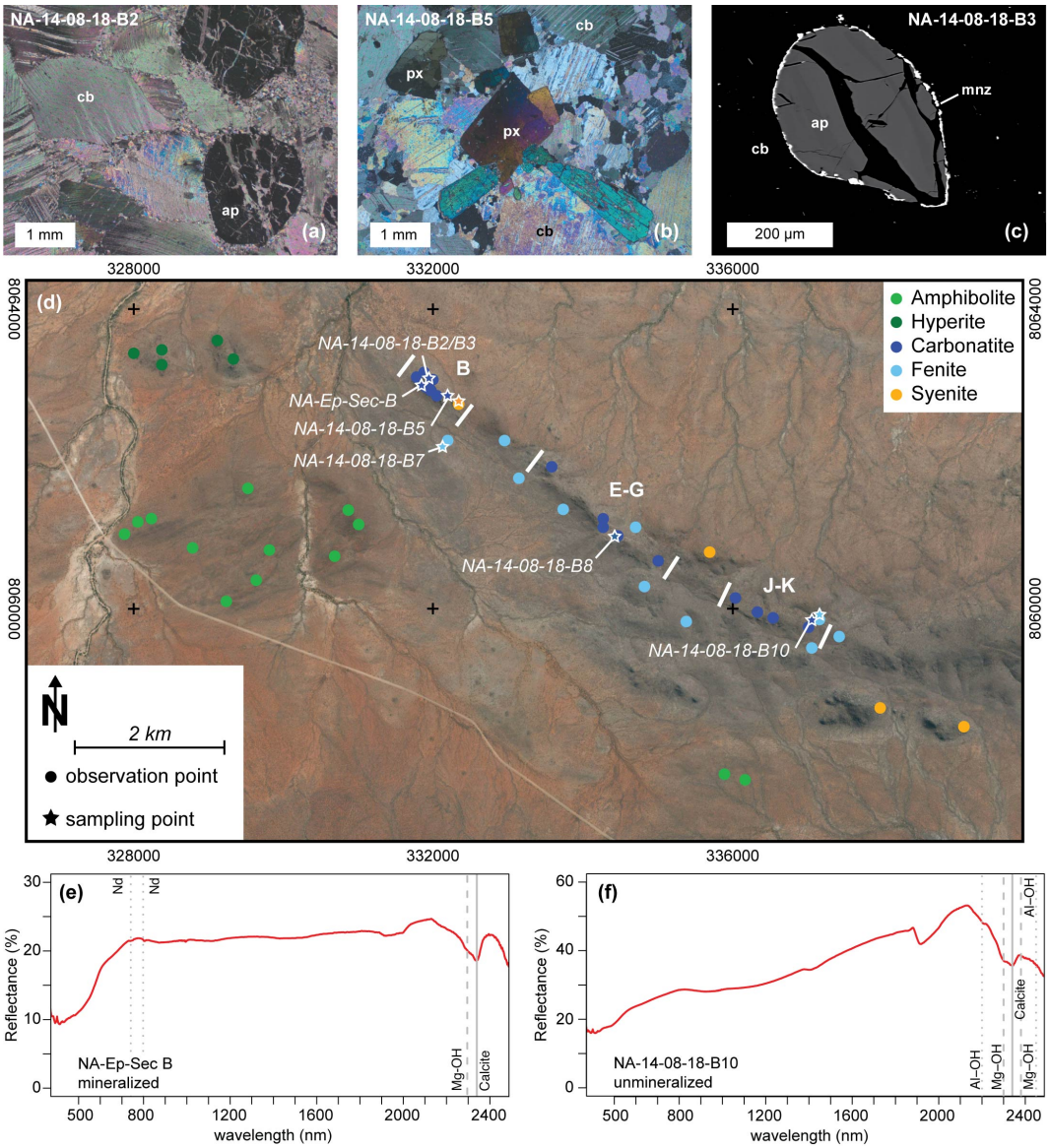

Figure 2. Validation sites for lithological mapping at Epembe dyke compiled from grab sampling [28], geological mapping [29] and our own field observations. (**a**,**b**) Thin section microphotographs (cross-polarized) showing fine to medium grained calcite-rich carbonatite with up to 3 mm long apatite (**a**) and pyroxene crystals (**b**); (**c**) BSE image of sample NA-14-08-18-B3 showing apatite with a monazite ring and fissure fillings; (**d**) Landsat 8 (true color R-G-B) B4-B3-B2 with points chosen for validation (points) and sampling points (stars). Names and the location of exploration sectors are also indicated. Coordinate system: WGS 84/UTM 33S; (**e**) Reflectance spectra of carbonatite sample NA-Epembe-Sec B from the northern high-grade zone with distinct absorption in the VNIR due to Nd^{3+} [33]; (**f**) Reflectance spectra of carbonatite sample NA-14-08-18-B10. Absorption features are marked at 0.741 and 0.798 µm for Nd^{3+}, 2.2 µm for Al-OH, 2.3 µm (and 2.5 µm) for Mg-OH and 2.34 µm for calcite. Mineral abbreviations: ap = apatite; cb = unspecified carbonate mineral; px = unspecified pyroxene.

Field and laboratory measurements of selected samples (see stars in Figure 2d–f) were carried out using a Spectral Evolutions PSR-3500 spectro-radiometer with a spectral range of 350 to 2500 nm. Reflectance spectra of all carbonatite samples show carbonate absorption features that are typical for calcite at 2.34 µm [34,35]. Rowan et al. [11] and Turner et al. [33] showed that narrow absorption bands in the VNIR- and SWIR-range are related to specific REE-elements (mostly Nd, e.g., 0.741 and 0.798 µm [33]). The lower detection limit for Nd^{3+} in high albedo samples is about 300 ppm [11]. Selected samples from inside (e.g., sample NA-14-08-18-B2, -B5, -Sec B, see Figure 2) and outside (e.g., sample -B8, -B10) the high-grade zones were studied in the laboratory. Spectra from the high-grade samples exhibit distinct features at 0.741 µm and 0.798 µm that correspond to Nd^{3+} absorption ([33]; see Figure 2e,f). However, the overall REE content (~0.5% TREO + Y) is low compared to other known carbonatite hosted deposits (e.g., up to 7.98 wt% TREO + Y as at Mountain Pass/USA [31]) and does not allow a direct detection of these absorption features in HyMap data, which will be described in Section 4.2.

In thin sections of these enriched samples, we observe crystals of apatite and pyroxene with a diameter of up to 3 mm (see Figure 2a,b). The matrix is mainly composed of carbonate minerals showing different stages of deformation and minor feldspar (microcline and plagioclase). SEM-EDX analysis indicates calcite as the dominant matrix material. SEM-based automated Mineral Liberation Analysis (MLA) by FEI Quanta 650F was applied to four polished thin sections of carbonatites (NA-14-08-18-B2, -B3, -B5, -B8; see Figure 2). REE bearing minerals and their textural association were detected by automated rare minerals search mode SPL (Selected Particle Listing) by SEM-EDX. We found relicts of monazite grains with replacement structures by allanite and synchysite. Especially the replacement of apatite by monazite and xenotime (ring structures around and fissure fillings in REE-rich apatite grains) indicate a strong post-magmatic overprint.

3.2. Fenite

Fenites are metasomatized country rocks in contact with igneous rocks (not exclusively a carbonatite-alkaline silicate rock association [36]). Their conversion to aegirine- and alkali-amphibole-rich rocks is induced by the K- and Na-contents of carbonatitic melts [36]. Fenitization is further characterized by a declassification of wall rocks, as well. Another common feature is the decomposition from An-rich fenites to Ab-rich and later to Or-rich compositions [36].

The Epembe dyke shows an irregular shape of fenite aureole at the margins of carbonatite and syenite that is more extensive to the south [23]. Different stages of metasomatism from highly altered grey syenite and wall rock to unaltered ones are evident. The syenite also shows fenitization and is entrained as xenoliths within the carbonatite. This indicates a later intrusion of carbonatite. A pinkish to reddish color is common and due to hematitization [23]. Completely fenitized gneiss is characterized by strong foliation and a medium-grained texture. In situ spectra show an Al-OH absorption at 2.2 µm related to the breakdown of feldspar into illite and/or a Mg-OH feature caused by chlorite, biotite and amphibole [37]. Depending on the grade of weathering, the iron absorption [37] around 1.0 µm becomes stronger.

3.3. Syenite

Syenite is present as small, isolated intrusions and xenoliths in the carbonatite showing a reddish to grey color [23]. Xenoliths and cross-cutting carbonatite dykes are a strong indicator that syenite is older. In the southern part, more syenite intrusions crop out than in the northern part of the dyke. Syenite mainly consists of nepheline, orthoclase, aegirine-augite and minor calcite [29].

The typical reflectance spectrum of fresh, unweathered syenite is nearly flat and lacks characteristic features. The spectral features of weathered syenite are similar to fenite in SWIR. In situ spectra exhibit a prominent Al-OH feature around 2.2 µm due to the breakdown of feldspars and a broad Mg-OH located around 2.35 µm [37].

4. Methods

A complete workflow including all datasets and methods used is shown in Figure 3. For lithological classification, several combinations of SRTM-derived data and HyMap hyperspectral data were used and evaluated.

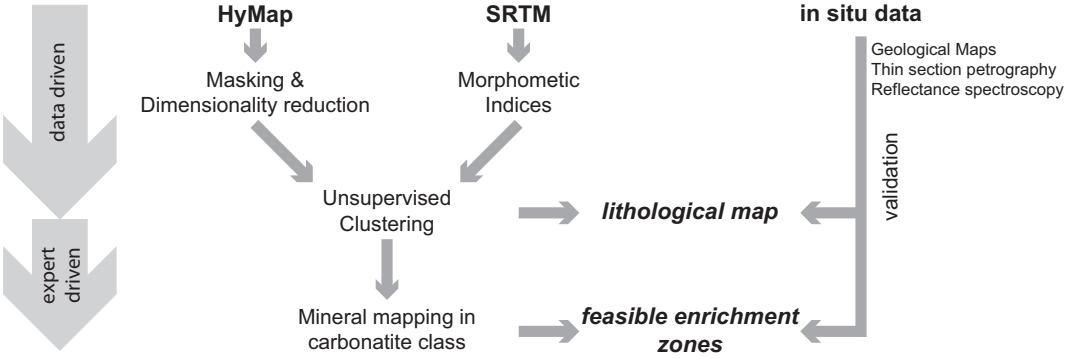

Figure 3. Flow-chart for the proposed processing. First Minimum Noise Fraction (MNF) transformed HyMap data, morphometric indices and spatial coordinates serve as input for unsupervised SOM clustering. In a second step, mineral mapping techniques and dedicated decision trees were applied to the carbonatite class obtained from the first step.

4.1. Morphometric Analysis

Morphometric indices were computed using 1 arc SRTM data with approximately 30-m spatial resolution. SRTM data were collected during the Shuttle Radar Topography Mission in 2000. Preprocessing includes depression fill and interpolation of no-data values.

Inferences on the geologic evolution and development of landscape can be drawn from a wide variety of indices ([38,39]). Morphometric indices can give important information on the surface expression of different rock types, which result in different morphologic landforms [40]. Thus, morphometric features can contribute to differentiating surface material with similar spectral properties. In the study area, e.g., calcrete and carbonatite might cause misclassification due to their spectral similarity. However, the carbonatite is located within the Epembe dyke, which is resistant to erosion and forms a prominent topographic ridge, while the calcretes form in the planar areas around the Epembe dyke.

The swath topographic profile can be used to describe complex landscapes. Elevation data from a rectangular swath are projected onto a vertical plane parallel to the long axis of the swath rectangle. Statistical parameters, such as mean, minimum and maximum, can be calculated therefrom. Curves for maximum and minimum elevations allow one to easily identify regional-scale planar surfaces [38]. Swath topographic profiles were calculated from 1-arc SRTM data over Epembe dyke. Swath orientation was set perpendicular to the trend of the dyke and the width was fixed to 10 km both to cover dyke and surfaces around and to avoid features oblique to the swath axis. Elevation data were sampled along 334 parallel profiles separated by 30 m.

The swath profile contributed to selecting the best suited set of indices and to set the size of the moving window used for index calculation. Each index can be used to highlight specific characteristics in morphology, e.g., ridges, tilted plateaus or different levels of erosion. Different sizes of moving windows enable one to highlight structures at specific scales. Small moving windows highlight, e.g., high-frequency structures, while large moving windows are best suited to highlight, e.g., major structures.

DEM-derived indices like the Topographic Position Index (TPI) [41] may provide information about the distribution of different lithologies. TPI was calculated using the TecDEM-toolbox [42].

The index describes the difference in elevation between the central pixel z_0 and the average elevation z_i in a predefined radius R [41]. It is computed with the equation:

$$TPI = z_0 - \frac{1}{n_R} \sum_{i \in R} z_i \quad (1)$$

If z_0 is higher than its average surrounding, the TPI is positive, and if its lower, TPI is negative. The TPI is also dependent on the moving window size R. A large moving window highlights regional-scale features, while a small moving window size is more suited for local topographic features [38]. TPI was calculated with a 50-pixel half-moving window size (ca. 1.5 km).

4.2. Pre-Processing of Spectral Data

HyMap is an airborne hyperspectral sensor that continuously covers the visible (VNIR) to short-wave infrared (SWIR) part of the spectrum between 450 and 2480 nm with an average bandwidth of 15 nm. Data were collected during the 2013 Kunene area survey with a flight altitude of 2000 m above ground level. This results in a spatial resolution of about 5 m. Prior to spectral processing, atmospheric correction to ground reflectance, including the effects of topography, was carried out by the HyVista Corp with a continental aerosol model and a mid-latitude summer atmospheric model (340 ppm total ozone and 75 km visibility). Pre-processing includes desmiling with a fifth-order polynomial function, followed by geometric correction and mosaicking. Furthermore, a composite mask as proposed by Cudahy et al. [43] was created:

1. green vegetation out: $NDVI > 0.25$,
2. dry vegetation out: normalized depth of the 2080-nm cellulose absorption feature from the continuum removal image (2000 nm + 2150 nm)/(2 × 2080 nm) ≥ 1.015 and
3. low albedo out: for reflectance at 1650 nm (Band 81) ≤ 10%.

A dimensionality reduction and noise filtering was performed using the Minimum Noise Fraction (MNF) transformation [44]. MNF is a type of principal component transformation ordering the data based on the signal-to-noise ratio [45]. It contains two steps: (1) noise suppression using the covariance matrix; (2) linear transformation of mutually uncorrelated pixels that have maximum variance.

4.3. Unsupervised Clustering by Kohonen Self-Organizing Maps

Unsupervised clustering by Kohonen Self-Organizing Maps (SOM) was chosen because a limited amount of field data for training and validation are available. SOMs can be used to segment and visualize similarities between diverse data types in a multi-dimensional space. It can be seen as a spatially-constrained form of k-means clustering [46]. The data-driven algorithm belongs to the group of unsupervised artificial neural networks and can handle non-linear relationships and non-Gaussian data distributions [47]. SOMs get trained by competitive learning and are perfectly suited for hyperspectral data analysis, as they outperform most unsupervised algorithms ([3,48,49]).

SOM clustering starts with selecting a random set a set of vectors $x = (x_1, x_2, ..., x_n)^T$, that are used to train the neural network. During training, those vectors are randomly compared to the data and adjusted to the most similar current training vectors. Not only the vector, but also the neighborhood is shifted. During training, the spatial extent of the neighborhood shrinks, and only the winning units are adopted in the end [46]. A detailed description can be found in Kohonen [47] and Bedini [3].

A cubic network geometry was chosen to cluster the data, as this is best suited for multi- and hyperspectral data [46]. The entirety of the data is classified by associating each input vector with the neuron having the closest synaptic weight vector (codebook vector). This codebook vector represents the mean spectrum for each class.

The SOM was performed on a two-dimensional 6 × 6 hexagonal grid, implemented in the Kohonen package [46] in the R software [50]. The learning rate η started at η_{max} = 0.05 and stopped at η_{min} = 0.01. During training, the size of the neighborhood decreased linearly [46]. The number of iterations was set to 100.

Spatial, spectral and geometric information were chosen as input: x- and y-coordinates, the first 20 MNF bands and TPI. The importance of spatial autocorrelation for machine learning algorithms was shown by Cracknell and Reading [6]: neighboring pixels are more related than those further apart. In Kohonen SOM clustering, the neighborhood decreases during training, so spatial dependencies can help to better train the synaptic weight vector. Spatial values in combination with physical properties can improve classification results by 5% to 10% [6].

4.4. Mapping Feasible Enrichment Zones

Each type of carbonatite (e.g., søvite and beforsite) yields a different level of enrichment [1]: with evolving type, REE content increases [51] while Nb-Ta decreases ([1,30]). Spectral unmixing and a decision tree were used to map specific internal zones within the carbonatite class obtained from lithological mapping. Sector B (location is indicated in Figure 2d) was chosen for a more detailed study because of known narrow enrichment zones and more available data due to exploration reports [23,28,29].

Carbonatites have specific spectral characteristics that can be used to differentiate them from surrounding rocks. The most characteristic feature is a sharp carbonate-related absorption between 2.32 to 2.34 µm, which varies depending on the relative Ca and Mg content of the carbonate mineral (e.g., [34,35,52]). The more Mg (i.e., dolomitic), the more the feature shifts to 2.32 µm [34,52]. Furthermore, a linear dependency of grain size, the position of absorption wavelength and absorption depth is recognized in the literature [35,52]. Thus, a decision tree (or hierarchical tree; [53]) approach was used in the original hyperspectral cube in the extensions of the carbonatite class to differentiate between dolomite and calcite dominant (beforsite and søvite, respectively). For this purpose, a binary decision rule was used: if the normalized absorption depth in Band 115 (2.3263 µm) is deeper than in Band 116 (2.3428 µm), the surface material is likely to be dolomite.

Multi-Range Spectral Feature Fitting (MRSFF, [54]) was used to identify zones enriched in Nb-Ta-LREE-bearing or indicator minerals (apatite and pyroxene; Mackay et al. [22]) within the carbonatite body. Input spectra were taken from Clark et al. [55] (USGS spectral library) for pyroxene (HS119.3B) and fluorapatite (WS416). Due to a lack of aegirine spectra in the available libraries, pyroxene spectra HS119.3B, described as augite [55], were chosen. Beside, it has a slightly different chemical composition compared to the aegirine endmember, and the spectral features are comparable. Spectra HS119.3B show features due to Fe^{2+}, as well as Fe^{3+}. The latter one is expected for aegirine, as well. The spectra were resampled to fit the original HyMap hyperspectral data cube. These minerals can be mapped due to a characteristic spectral signature and either contain high quantities of REEs (apatite) or are known to occur in enriched zones. MRSFF compares the spectral similarity of each pixel spectra to pre-defined segments of a reference spectra [54] and calculates the proportion of the respective minerals contained in the pixel. It matches the depth and shape of specific absorption features of the continuum removed spectra with the reference spectra using a least-square technique [54]. The output is a score image and a RMS (Root Mean Squared error) image with the fitting errors. Pixels with high RMS values were interpreted as false positives. Spectral ranges from 0.5 to 1.2 µm and 2.0 to 2.5 µm were selected for the MRSFF algorithm, because the most prominent absorption features for the reference spectra are in this region. However, MRSFF does not provide information on position and depth of absorption band [56], and thus, an in-depth mineralogical interpretation is not possible. A summary of possible indicator minerals and their related elements for Epembe is shown in Table 1.

Table 1. Indicator minerals for the Epembe deposit (compiled from Bull [23]). Apatite and pyroxene (augite instead of aegirine) were used for mineral mapping, as they have higher abundances in the enrichment zones and more pronounced features.

Mineral Name	Formula	Main Related Elements
Apatite	$Ca_5(PO_4)_3(OH,F,Cl)$	LREE, P
Aegirine	$NaFeSi_2O_6$	Nb, Ta, LREE
Monazite	$(Ce,La,Nd,Th)PO_4$	LREE, Th, P
Pyrochlore	$(Ca,Na)_2(Nb,Ti,Ta)_2O_6(O,OH,F)$	Nb, (Ta, U)

5. Results

5.1. Morphometric Analysis

A NNE-trending swath profile was drawn to show the main tectonic and topographic features (Figure 4). The swath profile shows that both the Epembe dyke and an anticline structure form two topographic ridges, which dominate a surrounding low-relief landscape. This low-relief topography (possibly an erosional planation surface) extends between the Zebra Mountains to the NNE and the Kaoko Mountains to the SSW. It is tilted towards the NE possibly as the result of normal faulting along the southern flank of the Zebra Mountains.

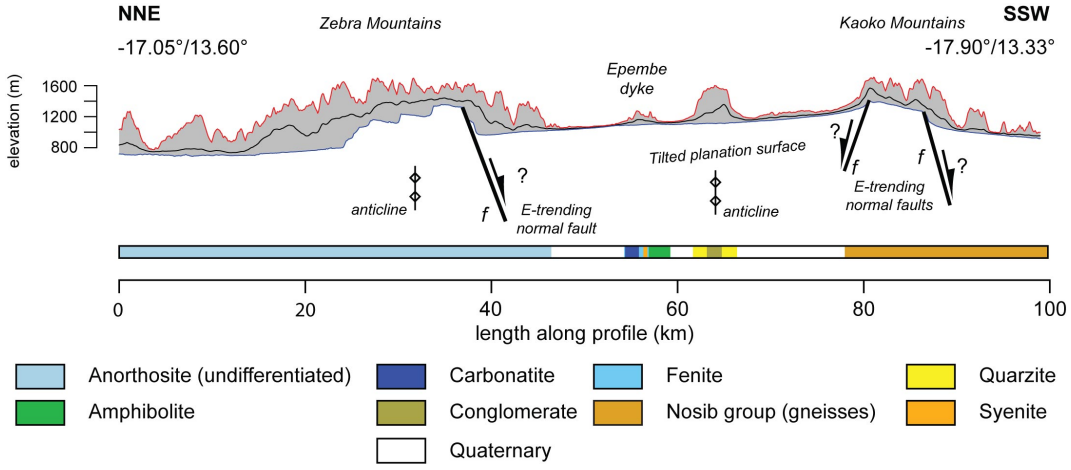

Figure 4. Topographic swath profile across Epembe dyke. Swath width was fixed to 10 km. Faults are indicated by *f*. Maximum, mean and minimum altitude are indicated as red, black and blue lines, respectively. The location is indicated in Figure 5.

The swath profile also shows that the topography of the Epembe syenite-carbonatite body is asymmetric with a steeper NE flank. The Epembe dyke displays three distinct ridges, which are associated with mapped geological SE-trending structures.

The Topographic Position Index (TPI, Figure 5) allows us to discriminate between the elevated ridges associated with the Epembe dyke and the surrounding low-relief topography (generally negative values). Conglomerate and quartzite show also positive values. However, they can be differentiated by spectral patterns. In order to highlight the relation between the topography and the lithology, we propose to compare the values of TPI for the main lithological units that are outcropping in this area (Figure 6). The distribution of TPI shows that the topography is mainly controlled by the lithology. Both carbonatite and syenite are associated with high TPI values that are significantly different from those of amphibolite and calcrete. They appear to be more resistant to weathering under arid conditions perhaps due to lack of chemical weathering and a higher density. Thus, they form most of the ridges and small hills. By contrast, amphibolite and fenite appear to be less competent, as they are associated with lower TPI values. Calcretes and gravels are associated

with low TPI values, as well (see Figure 6). These are weathering materials, which mainly occur within valleys and planar areas surrounding the topographic heights.

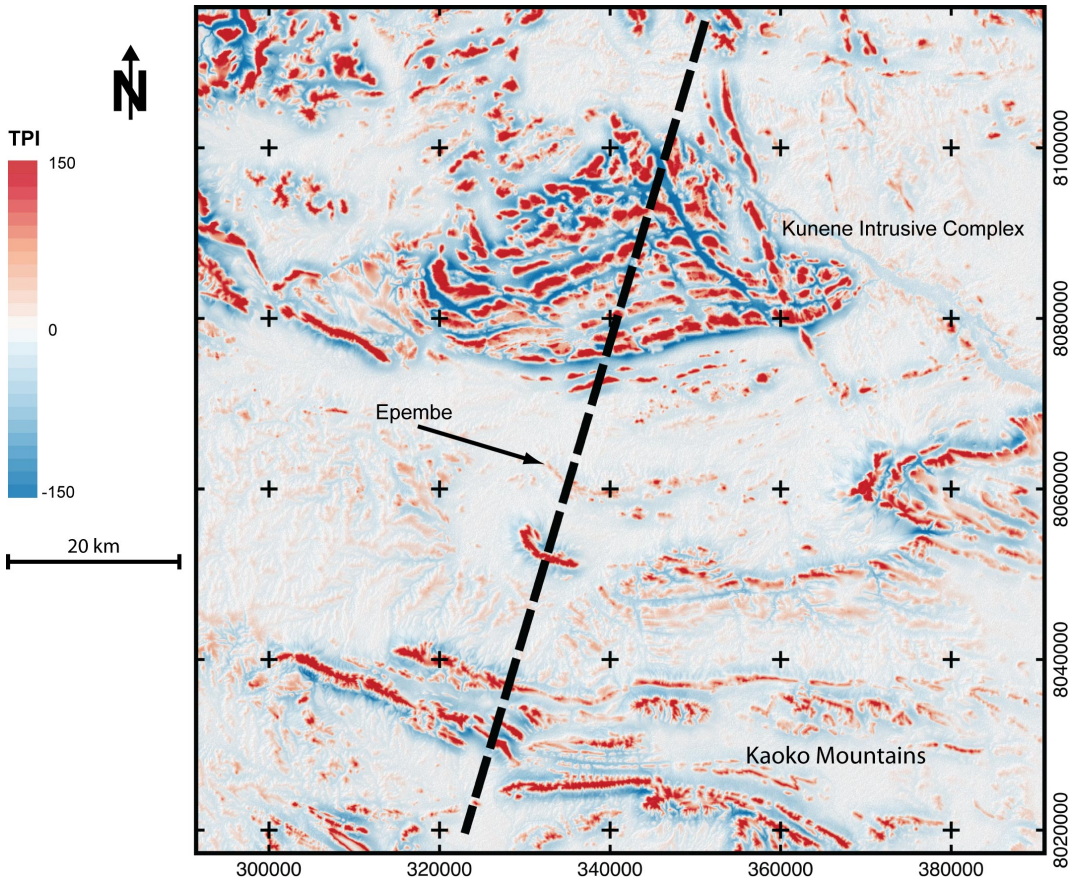

Figure 5. Topographic Position Index (TPI) calculated using a 100-pixel moving window. Higher values (red) indicate topographic heights, while low values represent plain areas. The location of the swath profile (see Figure 4) is indicated by a dashed line. Coordinate system: WGS 84/UTM 33S.

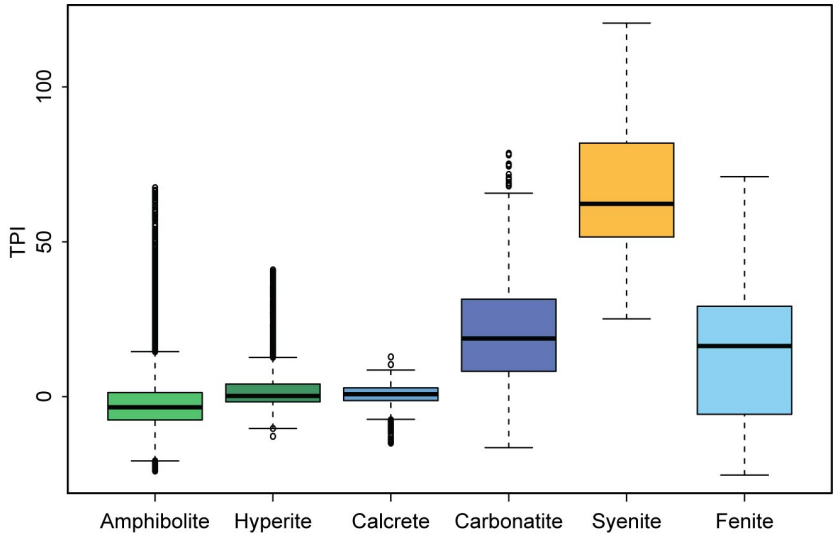

Figure 6. Boxplot of the TPI data of obtained classes from dataset containing TPI and spatial coordinates as input parameters. This clearly shows the dependence of lithology and morphology to better discriminate specific units.

5.2. Lithological Mapping

Results from SOM with different input layers are shown in Figure 7a–c. The respective labeled neurons for each spectral cluster are shown on the left side with the respective cluster spectra. Post-processing included merging of spectrally similar clusters and a sieving algorithm with a minimum of eight connected pixels and a five-pixel minimum group size followed by clumping with a 5 × 5 moving window to smooth the map and to delete small isolated fragments.

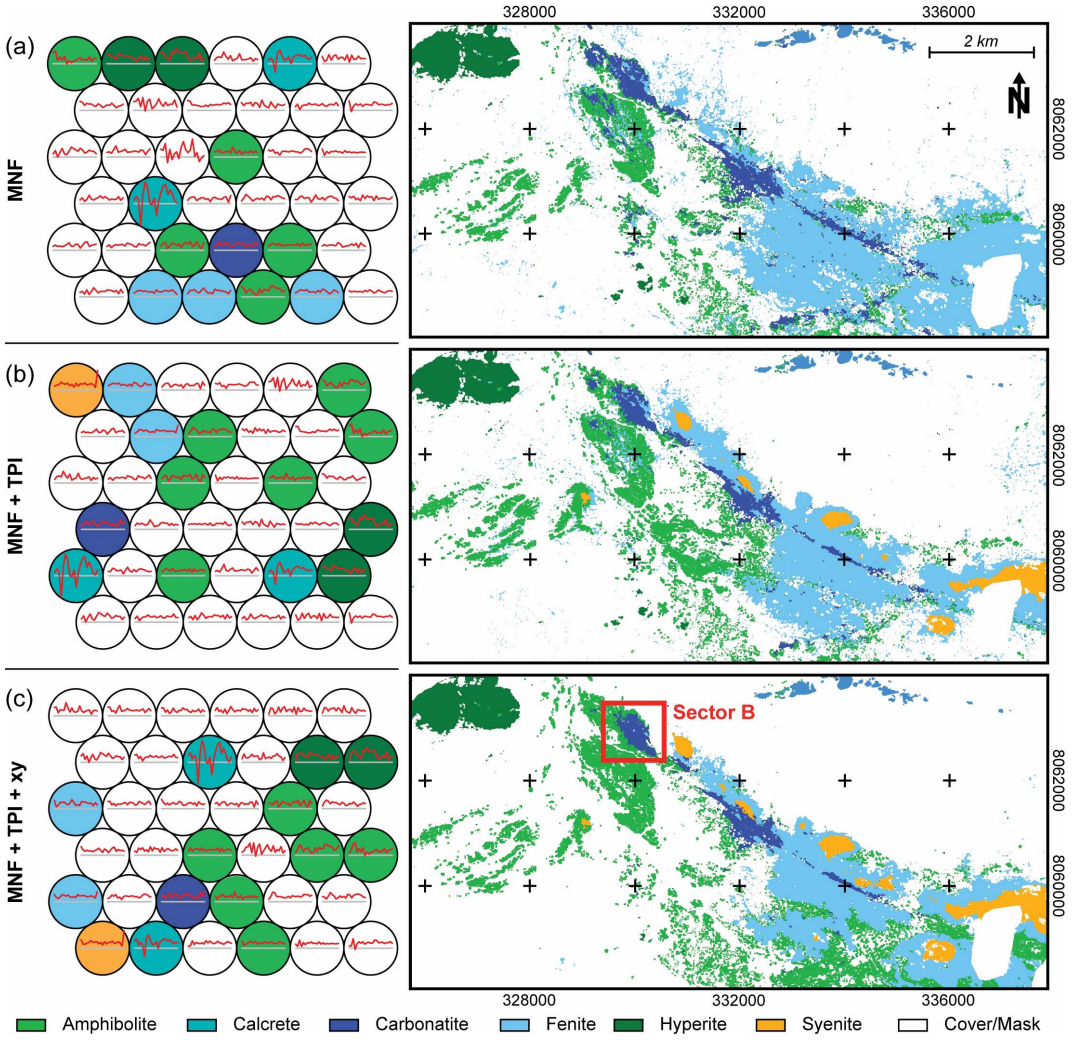

Figure 7. All parameter combinations allow us to map hyperite, amphibolite and fenite bodies. However, carbonatite, calcrete and syenite classes are not delineated using only the spectral data as input (see subfigure **a**). Only by including morphometric indices (TPI) and spatial information (xy-coordinates), these spectrally very similar lithologies are captured correctly (Subfigures **b**,**c**). In the following discussion, we will focus on the results where accuracy is highest (as will be discussed in the validation section).

The final seven classes represent the following lithological units: amphibolite, hyperite (pyroxenite), carbonatite, fenitization zone, calcrete and a mixed group for sedimentary cover and vegetation. Representative HyMap image spectra of these clusters/classes are shown in Figure 8. Lithologies were named according to the geological map of Namibia (Geological Survey of Namibia, Sheet Swaartbooisdrift, 2014).

The carbonatite class is limited to the NW-SE striking Epembe syenite-carbonatite composite body. In total, three major carbonatite bodies can be distinguished along the ridge: north, middle

and south, corresponding to exploration Sectors B, E to G and J to K (IBML, 2013). Spectra show a distinct carbonate absorption feature (at 2.34 µm) in the SWIR (see Figure 8). Furthermore, the ferric iron absorption feature is present in the VNIR range due to limonitic coatings. For the enrichment zones (as described by CoxsRocks [28] and discussed in Section 6.2), a small Mg-OH feature next to the calcite feature can be identified in the SWIR [37].

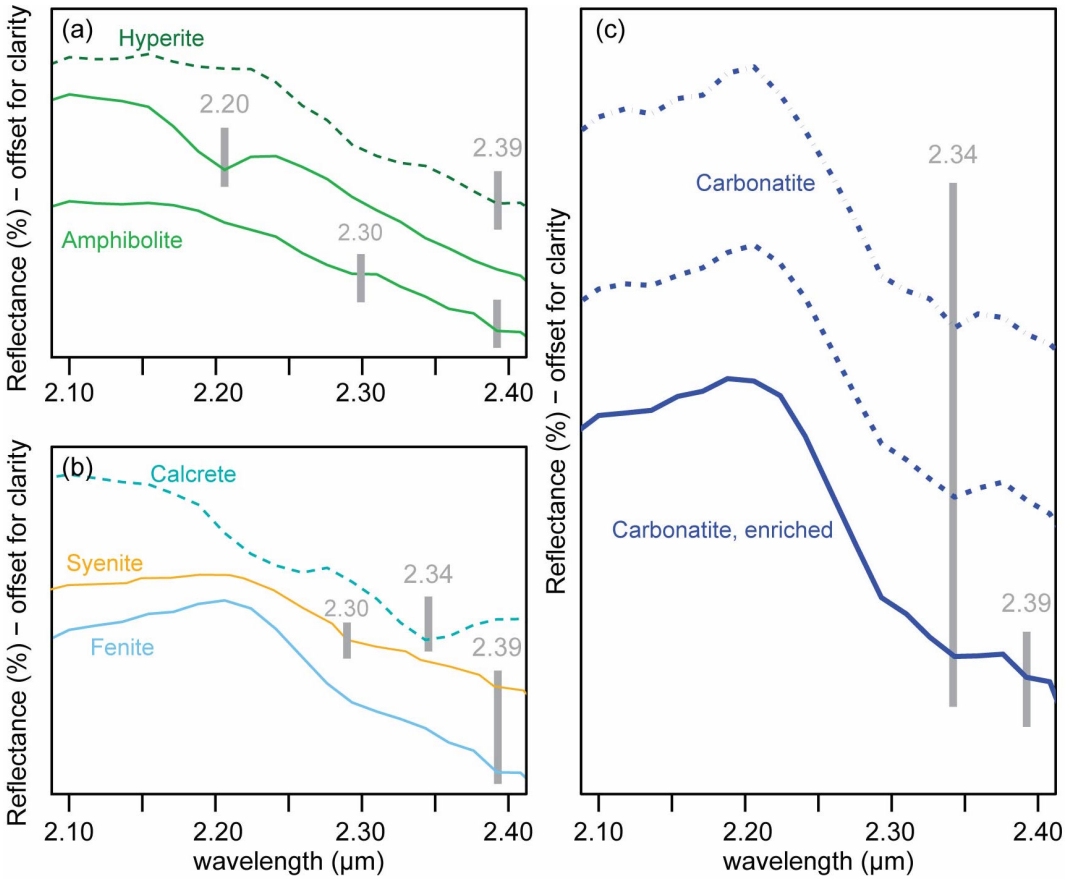

Figure 8. Representative HyMap SWIR pixel spectra for some of the clusters identified by unsupervised clustering of the dataset containing TPI and spatial layers (see Figure 7c). The spectra were offset for clarity. Absorptions at 2.34 µm can be assigned to calcite, ones at 2.20 µm to Al-OH and features around 2.30 and 2.39 µm to Mg-OH. (**a**) Image pixel spectra of mafic/ultramafic intrusions; (**b**) Image pixel spectra of fenite, syenite and calcrete; (**c**) Image pixel spectra of different carbonatite spots. Note that the stroke line is from the high-grade zone in Sector B.

The surrounding fenite alteration aureole shows an asymmetric shape around the carbonatite class. Morphologically, a gentle slope to the south and a step to the north of the carbonatite can be observed. The class is characterized by a strong Mg-OH absorption feature (Figure 8a). The rocks of the contact zone between fenite and the carbonatite core also show spectrally narrow CO_3^{2-} features. Those features fade out as one moves further outwards from the carbonatite.

Distinct syenite bodies were mapped close to the fenite class. The syenites have similar spectral signatures as the fenite (Figure 8b) with narrow Mg-OH absorption. However, they differ in their morphometric expression: syenite is slightly harder to erode and weathers to smoother forms than the fenite (see Figure 8b). This is why we are only able to correctly map this class by including morphometric indices.

Amphibolite forms the basement rocks and crops out south of the Epembe dyke. It is strongly eroded and now forms extensive plains. The amphibolite class is characterized by Mg-OH absorption features and frequently Al-OH around 2.20 µm (Figure 8a). Ferrous iron absorption is also visible in

the VNIR (around 1.0 µm [37]). Vegetation and soil cover is more abundant in this area, and the extent of the class is probably much larger beneath the soil cover. The distribution of the class remains nearly the same for all input band combinations.

The official geological map (Geological Survey of Namibia, 2014) shows a distinct hyperite body (pyroxenite) west of Epembe dyke. This feature is reproduced with all input data combination in terms of extent and shape. Absorption features of this class are caused by weathering of pyroxenes. Consequently, Mg-OH and Al-OH in the SWIR and ferric and ferrous iron in the VNIR are characteristic.

Areas with a flat morphology and a strong carbonate absorption in the SWIR occur north of the dyke in classification products. After a ground check, they were interpreted and classified as calcrete bodies (see Figure 8). This class shows the most pronounced difference between object and codebook vectors, indicating a higher within cluster variability of the spectra.

5.3. Validation of the Lithological Mapping Derived by SOM

A field campaign for validation and rock sampling was carried out in August 2014. Ten reference sites along the strike of the dyke were checked. These include seven sites for carbonatite, two for fenite and one for syenite. The location of each reference site was determined by handheld GPS measurements. Representative rock samples were taken from selected sites for further analysis. Validation data for all classes were compiled from high resolution geological mapping and sampling of previous investigators ([23,29]; see Figure 2).

The relationship between the reference information and our classification results is summarized in a confusion matrix calculated from the defined validation sites. The overall accuracy differs depending on the input datasets. The accuracy of the carbonatite class increases by 5% (see Table 2), when including TPI as an additional input parameter. TPI enhances the ridge-forming behavior, and thus, carbonatite and calcrete can be distinguished. Including spatial dependencies increases accuracy by another 5%. The highest overall accuracy (97.75%) was achieved by using TPI in combination with spatial coordinates and all MNF-bands. The respective confusion matrix is given in Table 3. Intrusions of syenite could only be discriminated using all variables, as the spectral similarity to fenite is very high. Results for this particular class do not agree with the geological map (as provided by Geological Survey of Namibia, 2014), but they corroborate field investigations and small-scale mapping [23]. For example, in the southern portion of the study area, more syenite intrusions outcrop than in the northern part of the dyke.

Table 2. Accuracy statistics for unsupervised classification using Kohonen self-organizing maps.

Input Parameters	κ	Overall Accuracy (%)
MNF	0.8270	88.2040
MNF + TPI	0.8833	92.0109
MNF + TPI + xy	0.9671	97.7537

Table 3. Confusion matrix for classification using MNF, TPI and spatial coordinates.

Class	Carbonatite	Hyperite	Amphibolite	Fenite	Syenite
Unclassified	0.00	0.02	0.01	0.07	0.00
Carbonatite	85.84	0.10	0.17	0.25	0.29
Hyperite	0.00	98.59	0.01	0.00	0.00
Amphibolite	0.00	1.28	99.69	3.12	0.00
Fenite	14.11	0.02	0.12	95.92	1.28
Syenite	0.05	0.00	0.00	0.63	97.43
Total	100.00	100.00	100.00	100.00	100.00

5.4. Mineral Mapping of Potential Enrichment Zones

Results for spectral unmixing of pyroxene and apatite are shown in Figure 9a,b and of the decision tree approach to distinguish between beforsite and søvite are shown in Figure 9c. At first glance, there seems to be an internal structure within the carbonatite dyke related to mineralogy and potential high-grade zones. These results need to be explored and validated in more detail with regard to Nb-Ta-REE enrichment.

Thematic mineral maps for apatite and pyroxene resulting from MRSFF show NW-SE trending zones with moderate to high score values for fluorapatite (Figure 9a) and pyroxene (Figure 9b). Medium RMS errors (<10%) are associated with those mineral mapping results due to the sensitivity of the spectral feature fitting algorithm for minor constituents. Computed "fit" (scale/RMS) images show similar patterns as the score values. These images are produced by dividing the score image by the RMS image. They can be interpreted as a measure of how well the spectra fits the hypercube. These "fit" images are standard procedures in ENVI. The higher the "fit" value, the higher the relative abundance of the mineral.

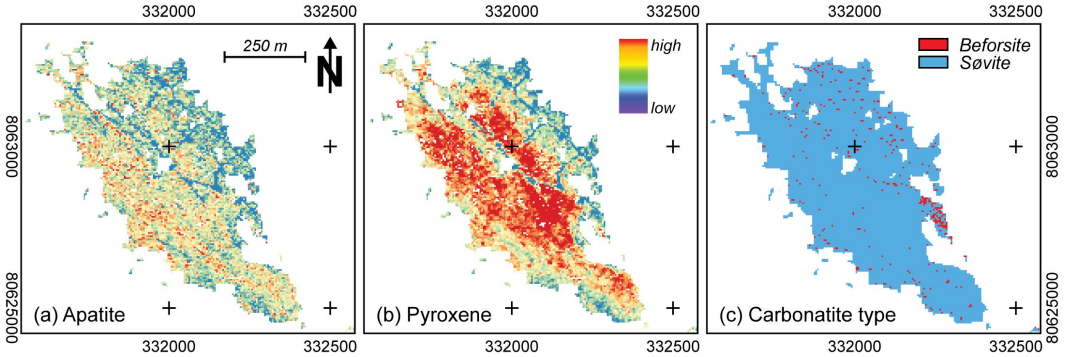

Figure 9. Detailed thematic maps of Sector B. The extent of the area is marked by a red rectangle in Figure 7c: (**a**,**b**) spectral feature fitting result for the accessory minerals in the carbonatite class: (**a**) fluorapatite; (**b**) pyroxene. Reference spectra taken from Clark et al. [55] (USGS spectral library) are HS119.3B and WS416, respectively; (**c**) Distribution of beforsite and søvite in the outcrop of Sector B based on hyperspectral data analysis with the decision tree approach. Coordinate system: WGS 84/UTM 33S

In order to interpret the calculated mineral abundance maps, we attempted to correlate the mineral scores with dose rates available from previous surveys [28]. A Pico Envirotech GRS-2 portable γ-spectrometer was used for data acquisition by Kunene Resources [28] in a sampling distance of 1 m perpendicular to the dyke and a line distance of 25 m. Simultaneously, the dose rates for the K-, Th- and U-channel and total counts were measured. However, counts for U and Th are overall not reliable due to unknown and suspicious calibration of the data and noise. Thus, just the total dose rate is used, as high dose rates are known to positively correlate with enrichment zones. Mineral indicators should show the same behavior. A positive correlation is to be expected if the method works well. Thresholding was applied to (a) the interpolated dose rates (using inverse distance weighting) and (b) the mineral maps to compare scores above 1.15 (pyroxene) with total dose rates higher than 180 (Figure 10b). Zones of high values show similar trends, and statistical correlation using Spearman's rank test results in a correlation coefficient of $R^2 = 0.388$ (pyroxene score vs. total counts). To further investigate the correlation between the two parameters, a profile across Sector B was drawn. Peaks in total counts and pyroxene score correlate with the high-grade zones from previous reports. The thresholded areas even coincide with two small ridges (see Figure 10) as the reported morpho-tectonic expression of the high-grade zones. A threshold of 0.65 was chosen for apatite. However, the apatite score does not provide significant correlation with total count rates

(R^2 = 0.157). This can be possibly explained by less distinct absorption features for apatite in the range of the HyMap sensor.

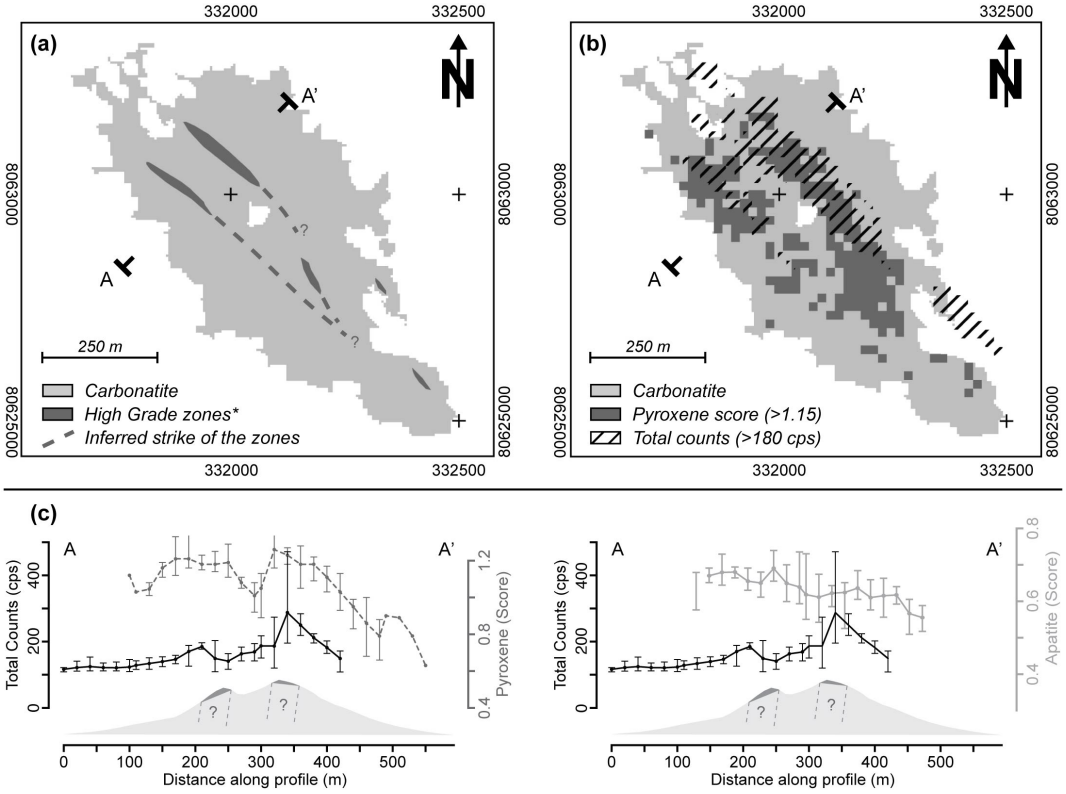

Figure 10. Validation of mineral mapping: (**a**) extension of the high grade zones * (based on own fieldwork in 2014 and 2016) within the extensions of the carbonatite (light grey); (**b**) Thresholded pyroxene score (>1.15) overlain by total counts (>180 cps) showing a spatial dependency of both indices. The extension of the carbonatite is indicated in lighter grays; (**c**) The graph below is showing the variation of total counts (cps), pyroxene (augite) and apatite score across Sector B. In the elevation profile, the high-grade zones are indicated, as defined by previous studies. Pyroxene (augite) score and total counts correlate and reproduce these zones well. Coordinate system: WGS 84/UTM 33S.

Taking into consideration the different spatial resolutions of the two datasets, as well as the low quality of the radiometric data, the obtained correlation between the total counts and the pyroxene score is a promising result to further test the mineral indices as the first tool for detecting enrichment zones.

6. Implications for the Exploration of Nb-Ta-REE-Hosting Carbonatite

6.1. Improving Lithological Mapping

Lithological classification with the aim of directly and accurately mapping the REE-Nb-Ta-bearing carbonatite is difficult due to the spectral similarity of the surrounding lithological units (especially the almost spectrally identical calcretes). We showed that this problem can be solved by including morphometric data as input datasets for classification. Therefore, we were able to increase classification accuracy by 10%. In the study area, unsupervised clustering using the SOM algorithm delivers good results for lithological mapping as described by the distance between object and codebook vectors. As the SOM algorithm tries to minimize the distance between the codebook vector and each training vector, the SOM similarity plot can be used as a kind of internal quality measure. The overall quality for the selected input band combination is good, as the distance between

objects and codebook vectors is low. Only the neurons labeled as calcrete are affected by a higher variance, due to a more inhomogeneous composition and scree cover. A larger SOM grid would lower the within cluster variability, and more lithological differences might be detected. In return, however, post-classification labeling of neurons will be more difficult and time consuming. A second clustering step of neurons and pruning of the number of classes using different approaches becomes more important in this context [57].

Our results clearly show that a good delineation of the target carbonatite can only be achieved by using a combination of spectral, morphometric and spatial information. For the Epembe carbonatite, this was done by including the Topographic Position Index (TPI) and spatial coordinates. Including the TPI allows one to distinguish between fenite and syenite, as these two lithological units exhibit different forms of weathering and, thus, morphology. Including spatial dependencies could further improve accuracy by 5% [6] as neighboring pixels are more likely to belong to the same class. However, in comparison, the carbonatite class shows lowest accuracy (∼86%; Table 3). This can be caused by scree cover, on the one hand, and by the fact that the marginal carbonatite zones are often characterized by fenite with carbonatite dykes.

6.2. Mapping Feasible Enrichment Zones

Based on the final results of lithological mapping, internal enrichment zones within the carbonatite class were mapped. Our approach is based on expert-knowledge about mineralogical and petrological relations that allow the definition of exploration proxies ([22]). Previous investigations ([23,28,29]) and our own field observations showed that Nb-Ta-LREE enrichment is assigned to a carbonatite variety containing remanent aegirine crystals, disseminated apatite and pyrochlore. Furthermore, Nb and Ta are known to be exclusively associated with pyrochlore, while LREE occur in apatite and monazite [28]. Furthermore, a positive correlation of Ta and U in pyrochlore group minerals [30] is known from the literature. We thus argue that pyroxene indices (i.e., aegirine or augite) can be used as a first exploration indicator in a geological setting like Epembe.

To strengthen these arguments, the results of mineral mapping were compared to the interpolated dose rates maps (total counts in cps). Here, we took advantage of a strong positive link between U + Th concentration and Nb, Ta and TREO (Total Rare Earth Oxide) in available geochemical data. These dependencies can be used as additional proxies for mapping potential enrichment zones by inexpensive mapping techniques.

It should also be noted that pyroxene-apatite-rich zones form small-scale ridges at the meter scale. This indicates that those zones are more resistant to weathering. Probably another indicator (e.g., a high resolution elevation model) could help with indicating probable zones of focused enrichment. This also demonstrates the need for higher spatial resolution in elevation and spectral data for more accurate mapping of probable enrichment zones.

Zones characterized by a higher abundance of dolomite can indicate either later intrusive stages ([1,51]) or hydrothermal alteration along shear zones. This dolomite-rich variety was linked to a progressive Nb/Ta/LREE enrichment [23], and thus, dolomite abundance can correlate with zones of economic importance. The relation to shearing and hydrothermal alteration is witnessed by high count rates in radiometry, as well. Previous studies [23] state a progressive Nb/Ta/LREE enrichment during a sequence of carbonatite intrusions. Later shearing affects/overprints just to a small proportion. This, however, is in contrast to field observations with much apatite, aegirine and pyrochlore in the flow bands and shear zones. There is a need for more detailed studies to resolve the relative timing between intrusion, enrichment and faulting.

The expert-knowledge proved to be very important for our study as indicator minerals could be successfully defined based on these known relationships: the spectrally characteristic pyroxene and apatite could be successfully used for spectral unmixing, and a shift in absorption features for calcite vs. dolomite was used to delineate the dolomite-rich zones. Uncertainties result from weathered surfaces and an inhomogeneous distribution of indicator minerals within carbonatite.

Problems and uncertainties induced by vegetation cover and scree cannot be ruled out, but minimized by (1) higher resolution data and (2) the combination of more information, like spectral, spatial and morphometric datasets.

7. Conclusions

In this study, we present a multi-step classification approach that was focused on correctly delineating the critical element-enriched Epembe carbonatite dyke and to map enrichment zones within the carbonatite body. Our results show that combining geomorphic and spatial information with spectral datasets cannot only improve classification results by 10%, but also allows one to distinguish between spectrally very similar classes (calcrete vs. carbonatite). The highest overall accuracy was achieved by using a combination of MNF, TPI and spatial coordinates as input data for lithological classification.

Internal structures of carbonatite sequences were successfully mapped using mineral mapping with indicator minerals (apatite and pyroxene) and dedicated decision trees (dolomite-rich zones). The resulting indicator maps show a good correlation of high pyroxene and apatite scores with radiometric data and a high coincidence of thresholded, thematic layers of total counts and pyroxene index (R^2 = 0.388). These zones correlate with the so-called high-grade zones that are well-known from previous exploration studies that included drilling. These results stress the importance of a priori expert-knowledge to (1) define the proper indicators for exploration; to (2) find meaningful thresholds and to (3) put results into the geological context for interpretation and validation.

In the future, datasets with higher spatial resolution could eventually allow a more precise mapping of minerals with less pronounced absorption features that are obliterated by noise. Perhaps a direct mapping of REE absorption features is possible. Furthermore, using high-resolution DEMs and derived morphometric indies in future studies might have a significant impact on the detection of small-scale pyroxene-apatite-bearing ridges found in the area.

Acknowledgments: The Helmholtz Institute Freiberg for Resource Technology is gratefully thanked for supporting and funding this M.Sc. project. The authors thank Georgios Barakos and Kunene Resources for sharing data and information about the Epembe prospect. HyMap data and Geological Maps are courtesy of Geological Survey of Namibia. We also thank Gabriel Unger for creating a 3D model of Epembe deposit showing excellently the relation between enrichment and shear zones. R.Z. thanks Thomas Heinig for assistance with SEM-MLA and Raimon Tolosana Delgado for assistance with R and geostatistics. We grateful acknowledge the reviews of David Turner and five anonymous reviewers for their helpful comments and suggestions to the manuscript.

Author Contributions: All authors contributed in a substantial way to the writing of the manuscript: R.Z. performed the analysis and interpretation of remote sensing and validation data. R.Z., M.B., L.A. and R.G. wrote and edited the manuscript. R.Z. and L.A. calculated and interpreted the morphometry and swath profile. Field work was conduced by R.Z., M.B. and R.G. in 2014. K.M. provided the data and relevant datasets, spread the discussion about regional geology and helped with logistical support. R.G. designed the research and supervised the study at all stages.

Conflicts of Interest: The authors declare no conflict of interest.

Abbreviations

The following abbreviations are used in this manuscript:

cps: counts per second EDX: Energy Dispersive X-ray analysis
HyMap: Hyperspectral Mapping sensor of HyVista
LREE: Light Rare Earth Elements (La-Gd)
MLA: Mineral Liberation Analyzer
MNF: Minimum Noise Fraction
SEM: Scanning Electron Microscope
SPL: Selected Particle Listing; a workflow to map minerals within a given gray-scale by MLA
SOM: Self-Organizing Maps

SRTM: Shuttle Radar Topography Mission
TPI: Topographic Position Index
TREO: Total Rare Earth Oxide

References

1. Jones, A.P.; Genge, M.; Carmody, L. Carbonate melts and carbonatites. *Rev. Mineral. Geochem.* **2013**, *75*, 289–322.
2. IBML. *IBML Annual Report*; Technical Report; International Base Metals Limited: Chatswood, NSW, Australia, 2013.
3. Bedini, E. Mapping alteration minerals at Malmbjerg molybdenum deposit, central East Greenland, by Kohonen self-organizing maps and matched filter analysis of HyMap data. *Int. J. Remote Sens.* **2012**, *33*, 939–961.
4. Van der Meer, F.D.; Van der Werff, H.M.; Van Ruitenbeek, F.J.; Hecker, C.A.; Bakker, W.H.; Noomen, M.F.; Van der Meijde, M.; Carranza, E.J.M.; de Smeth, J.B.; Woldai, T. Multi- and hyperspectral geologic remote sensing: A review. *Int. J. Appl. Earth Obs. Geoinf.* **2012**, *14*, 112–128.
5. Brandmeier, M.; Erasmi, S.; Hansen, C.; Höweling, A.; Nitzsche, K.; Ohlendorf, T.; Mamani, M.; Wörner, G. Mapping patterns of mineral alteration in volcanic terrains using ASTER data and field spectrometry in Southern Peru. *J. S. Am. Earth Sci.* **2013**, *48*, 296–314.
6. Cracknell, M.J.; Reading, A.M. Geological mapping using remote sensing data: A comparison of five machine learning algorithms, their response to variations in the spatial distribution of training data and the use of explicit spatial information. *Comput. Geosci.* **2014**, *63*, 22–33.
7. Swayze, G.A.; Clark, R.N.; Goetz, A.F.; Livo, K.E.; Breit, G.N.; Kruse, F.A.; Sutley, S.J.; Snee, L.W.; Lowers, H.A.; Post, J.L.; et al. Mapping advanced argillic alteration at cuprite, Nevada, using imaging spectroscopy. *Econ. Geol.* **2014**, *109*, 1179–1221.
8. Laakso, K.; Rivard, B.; Peter, J.; White, H.; Maloley, M.; Harris, J.; Rogge, D. Application of airborne, laboratory, and field hyperspectral methods to mineral exploration in the canadian arctic: Recognition and characterization of volcanogenic massive sulfide-associated hydrothermal alteration in the Izok lake deposit area, Nunavut, Canada. *Econ. Geol.* **2015**, *110*, 925–941.
9. Zimmermann, R.; Brandmeier, M.; Andreani, L.; Gloaguen, R. Hyperspectral remote sensing exploration of carbonatite—An example from Epembe, Kunene region, Namibia. In Proceedings of the Geophysical Research Abstracts, EGU, Vienna, Austria, 2–17 April 2015; Volume 17.
10. Jakob, S.; Gloaguen, R.; Laukamp, C. Remote sensing-based exploration of structurally-related Mineralizations around Mount Isa, Queensland, Australia. *Remote Sens.* **2016**, doi:10.3390/rs8050358.
11. Rowan, L.C.; Kingston, M.J.; Crowley, J.K. Spectral reflectance of carbonatites and related alkalic igneous rocks: Selected samples from four north American localities. *Econ. Geol.* **1986**, *81*, 857–871.
12. Bowers, T.L.; Rowan, L.C. Remote mineralogic and lithologic mapping of the ice river alkaline complex, British Columbia, Canada, using AVIRIS Data. *Photogramm. Eng. Remote Sens.* **1996**, *62*, 1379–1385.
13. Rowan, L.C.; Mars, J.C. Lithologic mapping in the Mountain Pass area, California, using Advanced Spaceborne Thermal Emission and Reflection Radiometer (ASTER) data. *Remote Sens. Environ.* **2003**, *84*, 350–366.
14. Bedini, E. Mapping lithology of the Sarfartoq carbonatite complex, southern West Greenland, using HyMap imaging spectrometer data. *Remote Sens. Environ.* **2009**, *113*, 1208–1219.
15. Mars, J.C.; Rowan, L.C. ASTER spectral analysis and lithologic mapping of the Khanneshin carbonatite volcano, Afghanistan. *Geosphere* **2011**, *7*, 276–289.
16. Boesche, N.K.; Rogass, C.; Lubitz, C.; Brell, M.; Herrmann, S.; Mielke, C.; Tonn, S.; Appelt, O.; Altenberger, U.; Kaufmann, H. Hyperspectral REE (Rare Earth Element) mapping of outcrops—Applications for neodymium detection. *Remote Sens.* **2015**, *7*, 5160–5186.
17. Neave, D.A.; Black, M.; Riley, T.R.; Gibson, S.A.; Ferrier, G.; Wall, F.; Broom-Fendley, S. On the feasibility of imaging carbonatite-hosted rare earth element deposits using remote sensing. *Econ. Geol.* **2016**, *111*, 641–665.
18. Haque, N.; Hughes, A.; Lim, S.; Vernon, C. Rare earth elements: Overview of mining, mineralogy, uses, sustainability and environmental impact. *Resources* **2014**, *3*, 614–635.

19. Simandl, G.; Akam, C.; Paradis, S. Which materials are 'critical' and 'strategic', British Columbia Geological Survey Paper 2015-3. In Proceedings of the Symposium on Strategic and Critical Materials proceeding; Victoria, BC, Canada, 13–14 November 2015; pp. 1–4.
20. Williams-Jones, A.; Wall, F.; Bau, M. Rare Earth Element Deposits. In Proceedings of the 13th Freiberg Short Course in Economic Geology, Freiberg, Germany, 8–12 December 2014.
21. Othman, A.A.; Gloaguen, R. Improving lithological mapping by SVM classification of spectral and morphological features: The discovery of a new chromite body in the Mawat Ophiolite Complex (Kurdistan, NE Iraq). *Remote Sens.* **2014**, *6*, 6867–6896.
22. Mackay, D.; Simandl, G.; Ma, W.; Redfearn, M.; Gravel, J. Indicator mineral-based exploration for carbonatites and related specialty metal deposits—A QEMSCAN® orientation survey, British Columbia, Canada. *J. Geochem. Explor.* **2016**, *165*, 159–173.
23. Bull, J. Detailed Geological Mapping and Petrological Study of the Ta-Na ± U Epembe Carbonatite-Syenite Complex in North-West Namibia. Master's Thesis, Camborne School of Mines, University of Exeter, Penryn, UK; 2013.
24. Maier, W.; Rasmussen, B.; Flechtner, I.; Li, C.; Barnes, S.J.; Huhma, H. The Kunene Anorthosite Complex, Namibia, and its satellite intrusions: Geochemistry, geochronology and economic potential. *Econ. Geol.* **2013**, *108*, 953–986.
25. Drüppel, K.; Littmann, S.; Romer, R.; Okrusch, M. Petrology and isotope geochemistry of the Mesoproterozoic anorthosite and related rocks of the Kunene Intrusive Complex, NW Namibia. *Precambrian Res.* **2007**, *156*, 1–31.
26. Brandt, S.; Will, T.; Klemd, R. Magmatic loading in the proterozoic Epupa Complex, NW Namibia, as evidenced by ultrahigh-temperature sapphirine-bearing orthopyroxene-sillimanite-quartz granulites. *Precambrian Res.* **2007**, *153*, 143–178.
27. Littmann, S.; Cook, N.; Teigler, B.; Drüppel, K. Ultramafic/mafic intrusives hosting Cu-Ni sulphide mineralisation, Itjitambi area, Kunene Region, N.W. Namibia: Investigation of drillcore, Hole OTD-1. *Communications of the Geological Survey of Namibia*, 2003.
28. CoxsRocks. *Independent Valuation Report—Epembe Rare Metals Project, Namibia (EPL3299)*; Technical Report; CoxsRocks Pty Ltd.: Perth, Australia, 2014.
29. Swinden, S. *Geological Mapping in Sectors B and K of the Epembe Dyke System: Results of Geological Mapping*; Technical Report; Swinden Geoscience Consultants: Wolfville, NS, Canada, 2014.
30. Hogarth, D. Pyrochlore, apatite and amphibole: Distinctive minerals in carbonatite. In *Carbonatites: Genesis and Evolution*; Bell, K., Ed.; Unwin Hyman: Boston, MA, USA, 1989; pp. 105–148.
31. Verplanck, P.; van Goseb, B.; Seal, R.; MacCafferty, A. *A Deposit Model for Carbonatite and Peralkaline Intrusion-Related Rare Earth Element Deposits*; U.S. Geological Survey Scientific Investigations Report; USGS: Denver, CO, USA, 2014.
32. Linnen, R.; Samson, I.; Williams-Jones, A.; Chakhmouradian, A. Geochemistry of the rare-earth element, Nb, Ta, Hf, and Zr deposits. In *Treatise on Geochemistry*; Elsevier: Amsterdam, The Netherlands, 2014; pp. 543–568.
33. Turner, D.J.; Rivard, B.; Groat, L.A. Visible and short-wave infrared reflectance spectroscopy of REE fluorocarbonates. *Am. Mineral.* **2014**, *99*, 1335–1346.
34. Gaffey, S.J. Reflectance spectroscopy in the visible and near-infrared (0.35 to 2.55 μ m): Applications in carbonate petrology. *Geology* **1985**, *13*, 270–273.
35. Zaini, N.; van der Meer, F.D.; van der Werff, H. Determination of carbonate rock chemistry using laboratory-based hyperspectral imagery. *Remote Sens.* **2014**, *6*, 4149–4172.
36. Le Bas, M.J. Fenites associated with carbonatites. *Can. Mineral.* **2008**, *46*, 915–932.
37. Hunt, G.; Salisbury, J.; Lenhoff, C. Visible to near-infrared spectra of minerals and rocks: III. Oxides and hydroxides. *Mod. Geol.* **1971**, *2*, 195–205.
38. Andreani, L.; Stanek, K.P.; Gloaguen, R.; Krentz, O.; Dominguez-Gonzalez, L. DEM-based analysis of interactions between tectonics and landscapes in the ore mountains and eger rift (East Germany and NW Czech Republic). *Remote Sens.* **2014**, *6*, 7971–8001.
39. Dominguez-Gonzalez, L.; Andreani, L.; Stanek, K.P.; Gloaguen, R. Geomorpho-tectonic evolution of the Jamaican restraining bend. *Geomorphology* **2015**, *228*, 320—334.

40. Grebby, S.; Cunningham, D.; Naden, J.; Tansey, K. Lithological mapping of the Troodos ophiolite, Cyprus, using airborne LiDAR topographic data. *Remote Sens. Environ.* **2010**, *114*, 713–724.
41. Gallant, J.; Wilson, J. Primary topographic attributes. In *Terrain Analysis: Principles and Applications*; Wilson, J., Gallant, J., Eds.; Wiley: New York, NY, USA, 2000, pp. 51–85.
42. Shahzad, F.; Gloaguen, R. TecDEM: A MATLAB based toolbox for tectonic geomorphology, Part 2: Surface dynamics and basin analysis. *Comput. Geosci.* **2011**, *37*, 261–271.
43. Cudahy, T.; Jones, M.; Thomas, M.; Laukamp, C.; Cacetta, M.; Hewson, R.; Rodger, A.; Verral, M. *Next Generation Mineral Mapping: Queensland airborne HyMap and Satellite ASTER surveys 2006–2008*; Technical report; CSIRO: Kensington, Australia, 2008.
44. Green, A.A.; Berman, M.; Switzer, P.; Craig, M.D. A transformation for ordering multispectral data in terms of image quality with implications for noise removal. *IEEE Trans. Geosci. Remote Sens.* **1988**, *26*, 65–74.
45. Boardman, J.W.; Kruse, F.A. Automated spectral analysis: A geological example using AVIRIS data, northern Grapevine Mountains, Nevada. In Proceedings of the Tenth Thematic Conference, Geologic Remote Sensing, San Antonio, TX, USA, 9–12 May 1994; pp. 407–418.
46. Wehrens, R.; Buydens, L.M.C. Self- and Super-organizing Maps in R: The kohonen Package. *J. Stat. Softw.* **2007**, *21*, 1–19.
47. Kohonen, T. *Self-Organizing Maps*, 3rd ed.; Springer Series in Information Sciences; Springer: Heidelberg, Germany, 2001, Volume 30.
48. Goncalves, M.L.; Netto, M.L.A.; Costa, J.A.F.; Junior, J.Z. An unsupervised method of classifying remotely sensed images using Kohonen Self-organizing maps and agglomerative hierarchical clustering methods. *Int. J. Remote Sens.* **2008**, *29*, 3171–3207.
49. Bedini, E.; Tukiainen, T. Using spectral mixture analysis of hyperspectral remote sensing data to map lithology of the Sarfartoq carbonatite complex, southern West Greenland. *Geol. Surv. Denmark Greenl. Bull.* **2009**, *17*, 69–72.
50. R Core Team. *R: A Language and Environment for Statistical Computing*; R Foundation for Statistical Computing: Vienna, Austria, 2014.
51. Smithies, R.; Marsh, J. The Marinkas Quellen Carbonatite Complex, southern Namibia, carbonatite magmatism with an uncontaminated depleted mantle signature in a continental setting. *Chem. Geol.* **1998**, *148*, 201–212.
52. Zaini, N.; van der Meer, F.D.; van der Werff, H.M. Effect of grain size and mineral mixing on carbonate absorption features in the SWIR and TIR wavelength regions. *Remote Sens.* **2012**, *4*, 987–1003.
53. Kruse, F.; Seznec, O.; Krotkov, P. Expert system for geologic mapping with imaging spectrometers. *Proc. SPIE* **1990**, doi:10.1117/12.21142.
54. Clark, R.N.; Gallagher, A.J.; Swayze, G.A. Material absorption band depth mapping of imaging spectrometer data using the complete band shape least-squares algorithm simultaneously fit to multiple spectral features from multiple materials. In Proceedings of the Third Airborne Visible/Infrared Imaging Spectrometer (AVIRIS) Workshop, Pasadena, CA, USA, 4–5 June 1990; Volume 90–54, pp. 176–186.
55. Clark, R.; Swayze, G.; Wise, R.; Livo, E.; Hoefen, T.; Kokaly, R.; Sutley, S. *USGS Digital Spectral Library Splib06a*; Digital Data Series 231; USGS: Denver, CO, USA, 2007.
56. Van der Meer, F.D.; De Jong, S. Spectral Mapping Methods: Many problems some solutions. In Proceedings of the 3rd EARSeL Workshop on Imaging Spectroscopy, Herrsching, Germany, 13–16 May 2003.
57. Cracknell, M.; Reading, A. Unsupervised clustering of continental-scale geophysical and geochemical data using Self-Organizing Maps. In Proceedings of the Third Australian Regolith Geoscientists Association Conference, Bunbury, Western Australia, 6–7 February 2014; pp. 20–24.